Heterostructured thin LaFeO3/g-C3N4 films for efficient photoelectrochemical hydrogen evolution

Vincent Guigoz, Lavinia Balan, Abdelhay Aboulaich, Raphaël Schneider, Thomas Gries

To cite this version:

Vincent Guigoz, Lavinia Balan, Abdelhay Aboulaich, Raphaël Schneider, Thomas Gries. Heterostructured thin LaFeO3/g-C3N4 films for efficient photoelectrochemical hydrogen evolution. International Journal of Hydrogen Energy, 2020, 45 (35), pp.17468-17479. 10.1016/j.ijhydene.2020.04.267 . hal-02884612

HAL Id: hal-02884612

https://hal.univ-lorraine.fr/hal-02884612v1

Submitted on 3 Dec 2020

Heterostructured thin $LaFeO_3$/g-C_3N_4 films for efficient photoelectrochemical hydrogen evolution

Vincent Guigoz [a,b], Lavinia Balan [c], Abdelhay Aboulaich [d], Raphaël Schneider [a,*], Thomas Gries [b,*]

[a] *Université de Lorraine, CNRS, LRGP, F-54000 Nancy, France*

[b] *Université de Lorraine, CNRS, IJL, F-54000 Nancy, France*

[c] *CEMHTI-UPR 3079 CNRS, Site Haute Température, 1D avenue de la Recherche Scientifique, 45071 Orléans, France*

[d] *Université Clermont Auvergne, Institut de Chimie de Clermont Ferrand UMR 6296 CNRS/UBP/Sigma Clermont, Campus des Cézeaux, TSA 60026-CS 60026, 63178, AUBIERE Cedex, France*

* Corresponding authors.

E-mail addresses: raphael.schneider@univ-lorraine.fr; thomas.gries@univ-lorraine.fr

Abstract

The deposition of $LaFeO_3$ at the surface of a graphitic carbon nitride (g-C_3N_4) film via magnetron sputtering followed by oxidation for photoelectrochemical (PEC) water splitting is reported. The $LaFeO_3$/g-C_3N_4 film was investigated by various characterization techniques including SEM, XRD, Raman spectroscopy, XPS and photo-electrochemical measurements. Our results show that the hydrogen production rate of a g-C_3N_4 film covered by a $LaFeO_3$ film, exhibiting both a thickness of ca. 50 nm, is of 10.8 $\mu mol.h^{-1}.cm^{-2}$ under visible light irradiation. This value is ca. 70% higher than that measured for pure $LaFeO_3$ and g-C_3N_4 films and confirms the effective separation of electron-hole pairs at the interface of $LaFeO_3$/g-C_3N_4 films. Moreover, the $LaFeO_3$/g-C_3N_4 films were demonstrated to be stable and retained a high activity (ca. 70%) after the third reuse.

Keywords

Lanthanum ferrite; graphitic carbon nitride; photoelectrochemical water splitting; hydrogen evolution

Introduction

Hydrogen (H_2) is a clean and carbon-free burning molecule and has become a promising candidate fuel as future energy carrier due to high energy density [1,2]. However, 96% of H_2 worldwide production originates from fossil fuels [3], which poses several environmental concerns such as the emission of a large amount of greenhouse gases such as CO_2, SOx, NOx and CO as by-products, which are mainly responsible of global warming issue. In addition to its environmental issues, most of H_2 production methods are highly energy consuming, which limits their application at very large scale. A big achievement would be to produce H_2 via an environmental-friendly and cost-effective method. In this regard, solar energy can be converted into H_2 by splitting water into oxygen (O_2) and H_2, storing the solar energy in the H-H chemical bond (artificial photosynthesis). Hydrogen photoproduction can be achieved by two means, photocatalytically via the irradiation of a catalyst in water or photoelectrochemically at the surface of a semiconductor electrode in three-electrodes cells in which the illuminated semiconductor electrode either oxidizes water into O_2 (photoanode) or reduces it into H_2 (photocathode) [4,5]. This photoelectrode is connected to a counter electrode that electrocatalyzes the respective half redox reaction.

Fujishima and Honda first demonstrated photoelectrochemical (PEC) water splitting for hydrogen production with a biased photoanode (titanium oxide, TiO_2) in 1972 [6]. To produce H_2 using PEC, the semiconductor material (photoelectrode) should have a suitable bandgap for water splitting half reactions to occur, absorb in the visible region of the solar spectrum, a high quantum efficiency (i.e. produce reactive charge carriers per absorbed photon) and a good photochemical stability (i.e. withstand photocorrosion) [7-10]. To reduce costs and environmental impact, the chosen material should also be abundant and non-toxic.

Most water splitting studies were conducted using wide bandgap semiconductors like TiO_2 or ZnO that can only be activated by UV light [11,12]. In recent years, intensive efforts were devoted to the extension of TiO_2 or ZnO visible light absorption and to the improvement of their photocatalytic properties via doping or building heterostructured catalysts in which the separation of charge carriers is improved [13–15]

Recently, lanthanum ferrite perovskite ($LaFeO_3$) has attracted a great attention [16-21], with applications in sensors [22], catalysts [23] and monitoring [24] due to its good chemical and thermal stability and its low toxicity. Moreover, $LaFeO_3$ has an advantageous optical bandgap, up to 2.1 eV, allowing the absorption of visible light until 590 nm. However, the photocatalytic activity of pure $LaFeO_3$ and its PEC performances are modest due to the fast recombination of photogenerated electron/hole pairs, to its weak charge collection, and to its low specific surface area [16,25–30]. Noteworthy is also that $LaFeO_3$ exhibits poor or no activity for H_2 photoproduction because its conduction band (CB) edge is close and too positive compared to that of the H^+/H_2 couple (0 V), which does not allow photogenerated electrons to reduce H^+ into H_2.

Heterostructured catalysts associating $LaFeO_3$ to reduced graphene oxide [31], TiO_2 [32,33] or graphitic carbon nitride ($g\text{-}C_3N_4$) [34-41] have received a much higher interest due to the improved separation of charge carriers. The organic $g\text{-}C_3N_4$ semiconductor is a highly promising material for photocatalytic applications like H_2 production, environmental remediation or CO_2 reduction into fuel molecules due to its low cost, its high thermal and chemical stability and its relatively low bandgap of ca. 2.7 eV allowing the absorption of visible light up to 460 nm [42-46]. Moreover, the energy positions of $g\text{-}C_3N_4$ valence band (VB) and of its CB are located at ca. 1.4 and -1.3 eV vs normal hydrogen electrode (NHE), making this semiconductor suitable for water splitting [42–45]. As $LaFeO_3$, $g\text{-}C_3N_4$ suffers from various drawbacks like a high recombination rate of charge carriers and a low charge mobility. Due to the adequate band edge positions of $g\text{-}C_3N_4$ and $LaFeO_3$, the coupling of these materials affords a Z-scheme charge transfer system which allows to promote the separation of electron/hole pairs and to extend the visible light absorption [30,34–41]. Xu *et al.* reported the preparation of a visible light active $LaFeO_3$ (5%)/$g\text{-}C_3N_4$ photocatalyst via a calcination process [34]. After association to 2% NiS used as co-catalyst and using triethanolamine as sacrificial substrate, a H_2 evolution rate (HER) of 121 µmol.g^{-1}.h^{-1} was obtained. Acharya *et al.* also described the mechanical synthesis of a $LaFeO_3$ (80%)/g-C_3N_4 catalyst exhibiting a HER of 1152 µmol.g^{-1}.h^{-1} using methanol as sacrificial substrate and 1% Pt as co-catalyst [41].

Herein, we report the first preparation of a thin $LaFeO_3$ film deposited on a g-C_3N_4 film for PEC water splitting. Spin-coating and magnetron sputtering, which are facile and scalable methods, were used to deposit g-C_3N_4 and $LaFeO_3$, respectively, to obtain heterostructured films. Photocurrent and HER measurements revealed that photocatalytic properties of $LaFeO_3$ were significantly improved after coupling with g-C_3N_4. A high HER value of 10.8 µmol^{-1}.h^{-1}.cm^{-2} was determined after 7 h under visible light irradiation. Moreover, 70% of the photocatalytic activity of the $LaFeO_3$/g-C_3N_4 were retained after the third cycle, indicating its good stability.

Experimental section

Synthesis and deposition of g-C_3N_4 on FTO

The g-C_3N_4 powder was synthesized by heat treatment of urea. Briefly, urea was placed in a crucible and stepwise heated at 250, 350 and 450°C for 1 h each with a heating rate of 10°C.min^{-1}. After cooling to room temperature, the pale yellow solid was grounded into powder.

Prior to any deposition, a transparent conductive oxide substrate, Fluorine doped Tin Oxide coated glass (FTO, TEC 7 Ω/sq, Solems) was successively washed with acetone and ethanol for ten minutes in an ultrasonic bath before drying with compressed air. g-C_3N_4 was dispersed in methanol at the concentration of 0.5 mg·mL^{-1} and ultrasonicated for 20 min. The dispersion was then left to rest for at least 4 days to let the largest particles to sediment. The concentration of the remaining lightweight exfoliated g-C_3N_4 in methanol was determined to be of ca. 0.10 mg·mL^{-1}. The dispersion was stable for months.

g-C_3N_4 nanosheets were deposited by dropping 10 µL of the previously prepared dispersion solution onto cleaned FTO and rotated at 500 rpm for 10 s. This step was repeated several times in order to control the g-C_3N_4 film thickness. Spin-coating was followed by a thermal treatment at 115°C on a hot plate for 30 min in air to evaporate methanol and assure good electrical contact.

Elaboration of $LaFeO_3$ thin film

LaFe films were deposited on pre-cleaned FTO or on g-C_3N_4 deposited on FTO by DC magnetron co-sputtering from two metallic targets: iron target (diameter: 50 mm, thickness: 0.25 mm, purity: 99.5%) and lanthanum target (diameter: 50 mm, thickness: 3 mm, purity: 99.9%). Two independent magnetrons focused at the centre of the substrate-holder and inclined by 30° with respect to the substrate normal were used with a target to substrate distance set equal to 10 cm. The base pressure in the sputtering chamber during deposition was 0.58 Pa in an atmosphere containing 10 vol.% H_2 – 90 vol.% Ar. The compositions of the thin films were controlled by the adjustment of the power applied to metallic target and stoichiometric LaFe films were obtained at 80 W on Fe target and 65 W on La target, respectively. Before deposition, a shutter was placed in front of the target to isolate the substrate during 5 min in order to remove native oxide layers. Thickness was controlled by adjusting the sputtering time. The substrate-holder rotated at 28 rpm during deposition to ensure homogeneity. Thin films were deposited without external heating and the deposition temperatures were below 50°C. At these temperatures, films remained amorphous and a post-annealing was performed to synthesize $LaFeO_3$ perovskite structure in a tubular furnace at 500°C for 2 h in air.

Characterization

The surface morphology of the films was imaged by a Philips XL30S-FEG scanning electron microscope (SEM). Film thicknesses were measured by SEM cross-section observation. The La/Fe atomic ratio was determined by energy dispersive spectroscopy (EDS). The crystallographic structure of the films was determined by X-ray diffraction (XRD) performed at room temperature using Bragg-Brentano θ/2θ measurements on a D8 Advance Bruker diffractometer (Cu Kα, λ = 1.54056 Å). Fourier transform infrared (FT-IR) spectra were recorded on an Agilent Cary 680 equipped with an attenuated total reflexion (ATR) element (resolution = 4 cm^{-1}). UV-visible absorption spectra were recorded on Cary 7000 UMS Agilent UV-visible spectrophotometer. Raman analyses were conducted using a Horiba Labram HR800 equipment with a 633 nm laser. All the optical measurements were performed at room temperature under ambient conditions.

X-ray photoelectron spectroscopy (XPS) analyses were performed on a Gammadata Scienta (Uppsala, Sweden) SES 200-2 spectrometer under ultra-high vacuum ($P < 10^{-9}$ mbar). The measurements were performed at normal incidence (the sample plane is perpendicular to the emission angle). The spectrometer resolution at the Fermi level is about 0.4 eV. The depth analyzed extends up to about 8 nm. The monochromatized Al Kα source (1486.6 eV) was operated at a power of 420 W (30 mA and 14 kV) and the spectra were acquired at a take-off angle of 90° (angle between the sample surface and photoemission direction). During acquisition, the pass energy was set to 500 eV for wide scans and to 100 eV for high-resolution spectra. CASAXPS software (Casa Software Ltd, Teignmouth, UK, www.casaxps.com) was used for all peak fitting procedures and the areas of each component were modified according to classical Scofield sensitivity factors.

The photoelectrochemical performance of as-prepared samples was measured in a three-electrode cell with Pt wire as the counter electrode, a saturated Ag/AgCl electrode as reference electrode and FTO glass coated with $LaFeO_3$ or $LaFeO_3/g\text{-}C_3N_4$ materials with a surface area of 1 cm^2 as the working electrode. A 0.1 M Na_2SO_4 (pH = 7) aqueous solution was used as electrolyte. All measurements were carried out under light illumination of 1 sun (100 $mW{\cdot}cm^{-2}$) provided by a 300 W Xe arc lamp fitted with an AM 1.5G filter. Linear sweep voltammetry (LSV) measurements were performed by scanning the potential from -0.8 V to 0 V vs Ag/AgCl at a scan rate of 5 $mV.s^{-1}$. Chronoamperometric measurements were recorded at a constant potential of -0.30 V vs the reference electrode by using a SP150 BioLogic potentiostat, cycling between dark and light illuminations of 30 s each for 10 min for evaluating photocurrent density.

Electrochemical Impedance spectroscopy (EIS) was performed for Nyquist measurements. Frequency range of 500 kHz - 1 mHz and magnitude of the modulation signal of 10 mV were used. Applied potential was -0.3 V vs Ag/AgCl under 1 sun illumination. Mott-Schottky spectra were acquired at frequencies from 6 kHz to 10 kHz in the potential range of 0.6 V to 1.6 V vs the reference electrode in the dark.

Hydrogen photoproduction

The photocatalytic hydrogen production test was performed in a sealed custom-made metallic photoelectrochemical cell with an attached quartz viewport using the irradiation conditions previously described. The whole system was filled with 0.1 M Na_2SO_4 (pH = 7) and purged with argon for 1 h before measurements. During the reaction, the amount of produced H_2 was determined with online quadrupole mass spectrometer (MS, Inficon Transpector MPS 100) operating with Ar as carrier gas. Measurements were realized at an interval of 1 h and averaged over 2 min.

Results and discussion

Materials characterization

$LaFeO_3$/g-C_3N_4 films on FTO were prepared using a three steps process depicted in Fig. 1. First, exfoliated g-C_3N_4 was coated on FTO via spin-coating. Next, La and Fe were deposited at the surface of g-C_3N_4 by DC magnetron co-sputtering. Finally, crystalline $LaFeO_3$ was produced by air oxidation of La-Fe films at 500°C for 2 h.

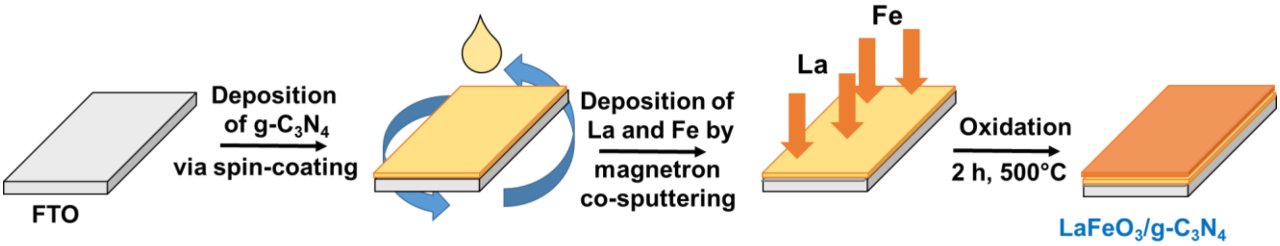

Fig. 1. Schematic illustration of the $LaFeO_3$/g-C_3N_4 film synthesis on FTO.

In order to reveal the structure, the composition and the morphology of the prepared samples, SEM, FT-IR, XRD and XPS analyses were conducted. Due to the high roughness of the FTO support, g-C_3N_4 and $LaFeO_3$ layers could not be observed by SEM (Fig. S1 and 2). The associated EDS mappings (Fig. 2) show that g-C_3N_4 and $LaFeO_3$/g-C_3N_4 films are homogeneously distributed at the surface of FTO. The La/Fe ratio in La-Fe and $LaFeO_3$ films is of ca. 1.0 and the La/Fe/O ratio in the $LaFeO_3$ film is of 1.0/1.0/3.0 (Fig. S2), which indicates the successful deposition of the $LaFeO_3$ film at the surface of g-C_3N_4. When the same deposition process was conducted on Si instead of FTO, thicknesses of 50 and 100 nm could be determined by SEM for g-C_3N_4 and $LaFeO_3$ layers (Fig. S3), respectively, which further confirms the efficiency of the magnetron co-sputtering method for the preparation of hierarchically structured films.

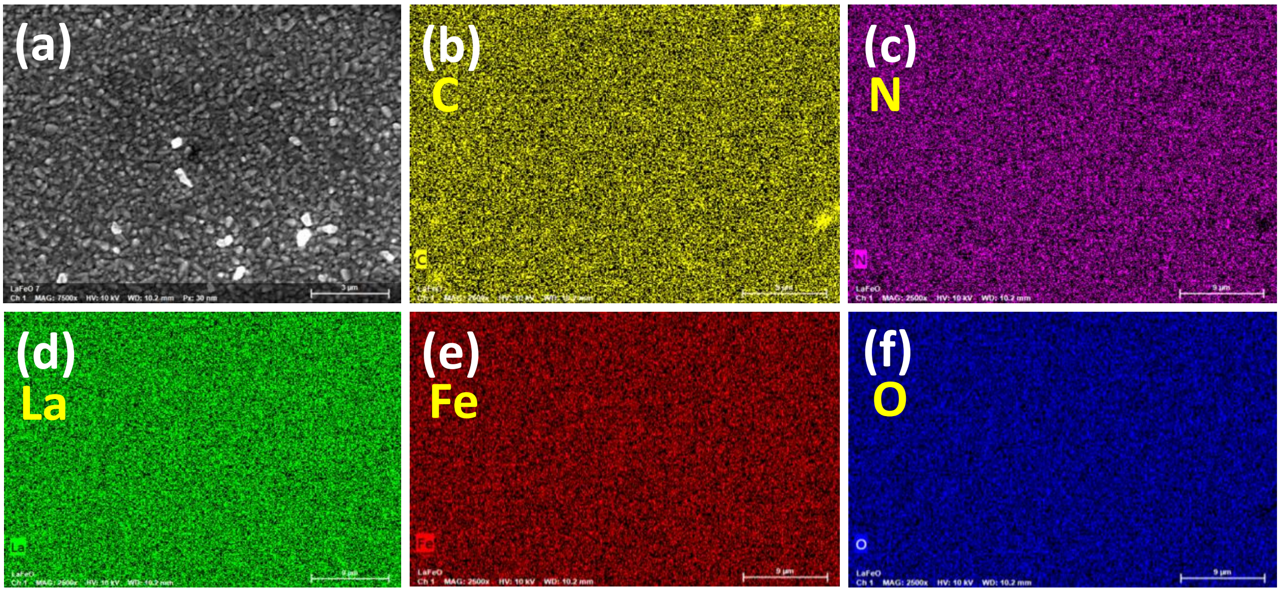

Fig. 2. (a) SEM image of $LaFeO_3$/g-C_3N_4 on FTO and EDS elemental mapping of (b) C, (c) N, (d) La, (e) Fe and (f) O.

Fig. 3a shows the FT-IR spectra of pure g-C_3N_4 and of $LaFeO_3$/g-C_3N_4 on the FTO surface. For g-C_3N_4, the bands observed between 1625 and 1200 cm^{-1} can be ascribed to C-N and C=N bonds stretching vibrations while signals appearing at 1250 and 1205 cm^{-1} correspond to the C-NH-C stretching vibration between heptazine units [44,49]. The sharp signal located at 810 cm^{-1} corresponds to the bending vibration of triazine units [46-50]. The peaks of g-C_3N_4 disappear after deposition of $LaFeO_3$. The signal at 541 cm^{-1} is the characteristic stretching vibration of the Fe-O bond in the octahedral FeO_6 of crystalline $LaFeO_3$ [51]. The two signals observed at 1469 and 1406 cm^{-1} can be attributed to the splitting of the ν_3 asymmetric stretching of La or Fe carbonates present at the surface of the film [52].

The powdered g-C_3N_4 shows a characteristic peak at 2Θ = 26.5° corresponding to the (002) plane and associated to the interlayer stacking of the conjugated aromatic systems (interlayer distance (d) of 0.32 nm) (Fig. 3b) [53]. The intensity of the g-C_3N_4 peak after deposition via spin coating on FTO is low compared to the signals of the substrate due to the weak amount of g-C_3N_4 present at the FTO surface (estimated to be ca. 1 µg per cm^2). The thickness of the g-C_3N_4 layer is of ca. 50 nm compared to the 600 nm thickness of FTO. The signal of g-C_3N_4 can be better observed after deposition on a Si substrate (Fig. S4). Finally, the peaks of $LaFeO_3$ deposited on g-C_3N_4 can be indexed to the orthorhombic structure (JCPDS No 00-037-1493) [54]. The co-existence of the peaks related to $LaFeO_3$ and g-C_3N_4 confirms the presence of these two materials on the FTO substrate and indicates that the g-C_3N_4 layer is stable after the oxidative treatment following the deposition of La and Fe by magnetron co-sputtering.

Raman spectroscopy was also used to examine the structural phase of the materials prepared (Fig. 3c). For pure $LaFeO_3$, La vibrations can be observed below 200 cm^{-1} while signals observed at 301 and 433 cm^{-1} correspond to A_g and B_3g modes, respectively. These values are in good agreement with those described in the literature for the orthorhombic structure of $LaFeO_3$ [26]. The other peaks observed may originate from structural defects (cation or oxygen vacancies). The strong signal appearing at 625 cm^{-1} likely originates from two-phonon scattering and/or impurities as previously reported [55]. After deposition of $LaFeO_3$ on g-C_3N_4, signals corresponding to CN heterocycles appear in the Raman spectrum [56], further confirming the successful association of g-C_3N_4 with $LaFeO_3$.

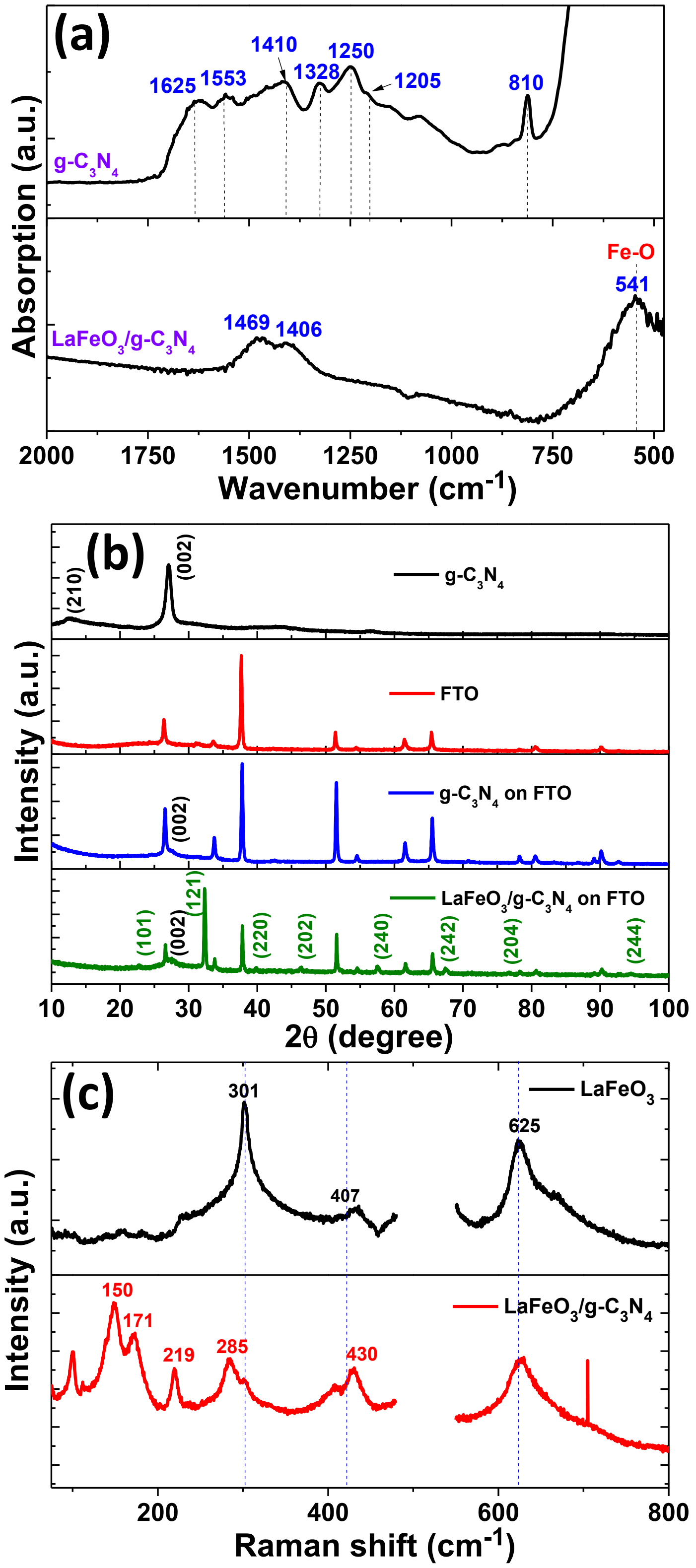

Fig. 3. (a) FT-IR spectra of g-C_3N_4 and of $LaFeO_3$/g-C_3N_4 deposited on FTO,

(b) XRD patterns of g-C_3N_4, FTO, g-C_3N_4 on FTO and $LaFeO_3$/g-C_3N_4 on FTO and (c) Raman spectra of $LaFeO_3$ and g-C_3N_4 deposited on Si substrate.

The surface chemical composition and the oxidation states of the elements in the $LaFeO_3$/g-C_3N_4 film were characterized by XPS (Fig. 4 and Fig. S5). The XPS survey spectrum of the film shows only the presence of La, Fe, O and C elements. The signal of N 1s could not be detected due to the thick layer of $LaFeO_3$ at the surface of g-C_3N_4 (the penetration depth of XPS, ca. 10 nm, does not allow reaching the g-C_3N_4 layer). The peaks of Fe $2p_{3/2}$ and Fe $2p_{5/2}$ are located at 711.60 and 724.02 eV, respectively, values corresponding to the core level spectra of Fe^{3+} cations included in a oxide (Fig. 4a) [28,41]. The high resolution XPS spectrum of La 3d shows signals at 855.40 and 838.59 eV corresponding to the spin-orbit splitting of La $3d_{3/2}$ and La $3d_{5/2}$ (Fig. 4b) [41,57]. The binding energies also confirm that La is present in the +3 oxidation state and incorporated in an oxide. The O 1s peak can be deconvoluted into two signals located at 529.68 and 531.65 eV which can be attributed to O atoms in the $LaFeO_3$ crystal lattice (La-O and Fe-O bonds) and to chemisorbed O containing species at the surface of $LaFeO_3$, respectively (Fig. 4c). Finally, the three peaks located at 285.0, 286.60 and 289.02 eV likely originate from carbon contaminants located at the surface of the $LaFeO_3$/g-C_3N_4 film (Fig. 4d).

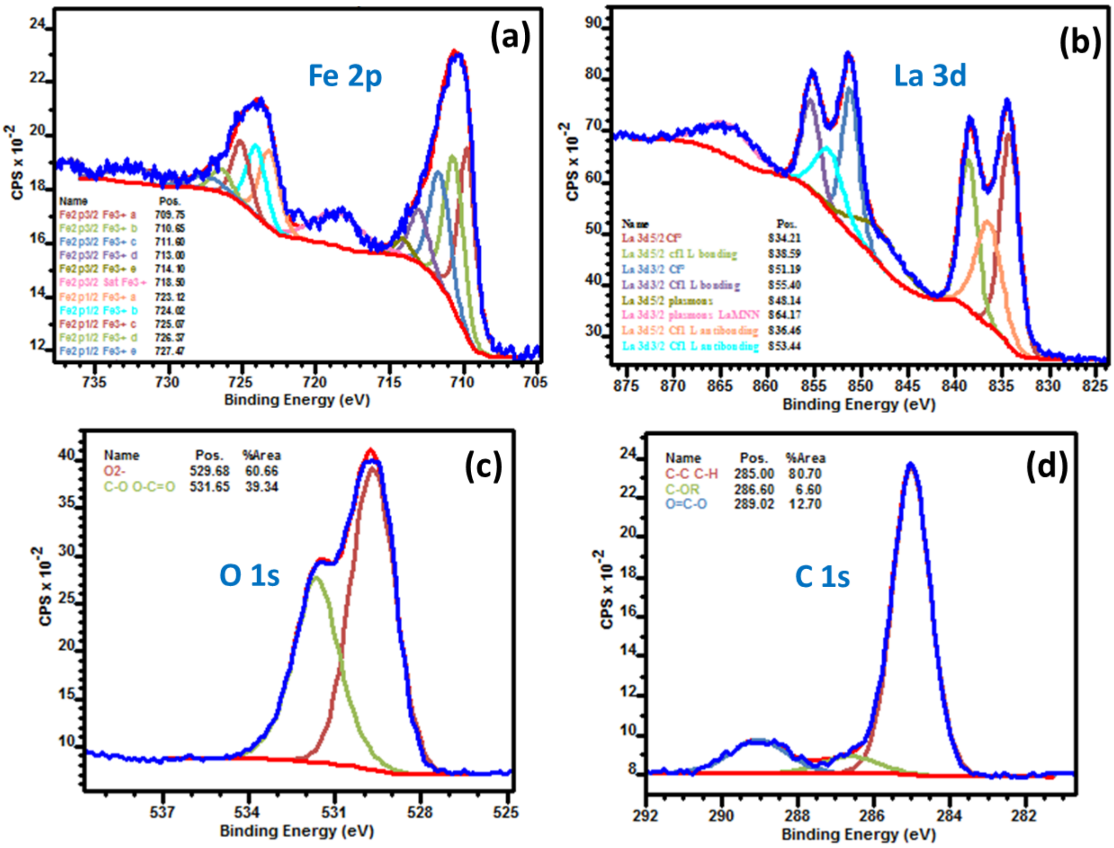

Fig. 4. High resolution XPS spectra of (a) Fe 2p, (b) La 3d, (c) O 1s and (d) C 1s for the $LaFeO_3$/g-C_3N_4 film.

Optical and electrochemical measurements

The UV-visible absorption spectrum of the pure 50 nm-thick $LaFeO_3$ film is presented in Fig. 5a. The optical bandgap (Eg) was determined using the Tauc/David-Mott model, by plotting $(\alpha hv)^{1/n}$ vs. hv, where h is Planck's constant, α is the absorption coefficient γ is the photon frequency and n is 1/2 for direct allowed transitions or 2 for indirect allowed transition [58]. The Eg value was estimated by extrapolating the linear region of the plot onto energy axis (insets of Fig. 5a). The absorption spectrum clearly shows two absorption edges, located at approximately λ_1 = 350 nm and λ_2 = 480 nm. The optical properties of $LaFeO_3$ were studied by Scafetta et al. using the density functional theory (DFT) [59]. The lowest bandgap was demonstrated to originate from a direct forbidden transition. Applying the same model to the present experimental data, a bandgap of ca. 2.28 eV was determined. This value is in good agreement with those described in the literature for nanocristalline $LaFeO_3$ [59,60]. A similar approach was also been used to determine the higher indirect transition at ca. 3 eV. The high absorption in the visible region originating from the electronic transition from the valence band to the conduction band (O 2p → Fe 3d) [17] should be beneficial for the photocatalytic activity under simulated solar light irradiation. Similar optical features were observed for the $LaFeO_3$ film deposited on g-C_3N_4 (Fig. 5b).

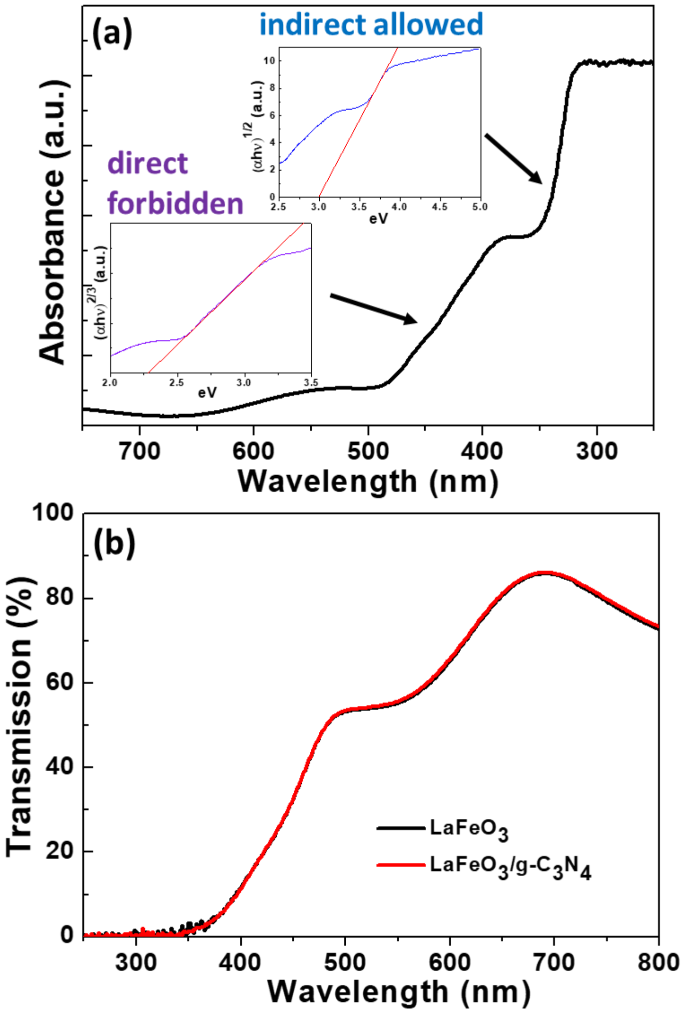

Fig. 5. UV-visible optical absorption spectrum of (a) a 50 nm-thick $LaFeO_3$ film on FTO (the insets show the Tauc plots for a direct-forbidden and indirect-allowed model for the first and second transitions, respectively). (b) $LaFeO_3$/g-C_3N_4 film.

Electrochemical impedance spectroscopy (EIS) measurements were conducted to determine the $LaFeO_3$ flatband potential. Fig. 6 shows the Mott-Schottky plots for $LaFeO_3$ thin film at different frequencies in the dark. The negative slope indicates that $LaFeO_3$ behaves as a p-type semiconductor. The flatband potential was estimated using the following Mott-Schottky equation for p-type semiconductor [61]:

$$(\frac{1}{C})^2 = \frac{2}{\varepsilon_r \varepsilon_0 A^2 e N_D}(V - V_{fb} - \frac{k_B T}{e}) \quad (1)$$

where C is the capacitance, e is the electronic charge, ε_r is the relative permittivity of materials, ε_0 is the permittivity of vacuum, N_D is the carrier concentration, k_B is the Boltzmann's constant, T is the absolute temperature, A is the area of electrode, V is the applied potential and V_{fb} is the flatband potential. Therefore, the flatband potential can be obtained by extrapoling the linear portion of the Mott-Schottky plot to V axis. A similar potential of +1.47 V vs Ag/AgCl was obtained for each applied frequency. The measured flatband potential can be converted to the RHE scale using the Nernst equation:

$$V_{RHE} = V_{Ag/AgCl} + 0.197 + 0.059 \cdot pH \quad (2)$$

and was determined to be 2.08 V vs NHE.

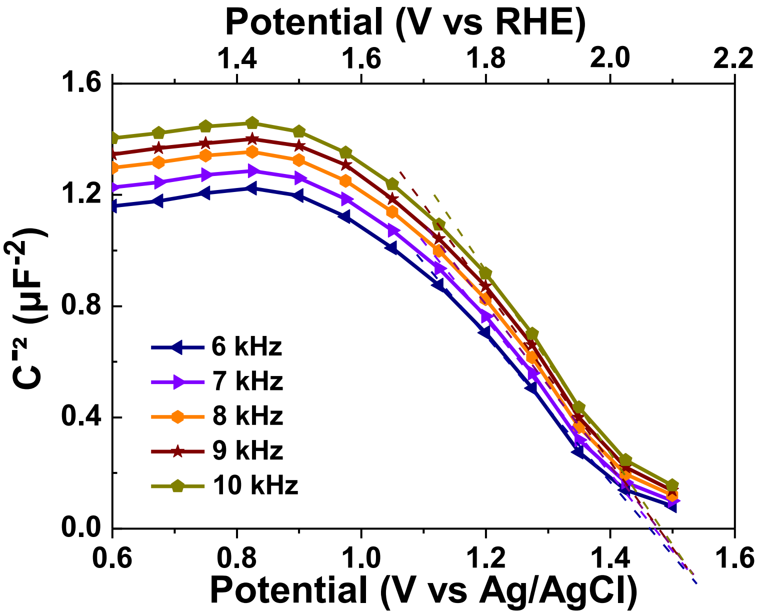

Fig. 6. Mott-Schottky plots for $LaFeO_3$ film (50 nm) at different frequencies determined from EIS measurements in the dark, in Na_2SO_4 (pH = 7).

Assuming in first approximation that the flatband potential of a p-type semiconductor is very close to the valence band (VB) edge position [52], the valence band maximum (VBM) of $LaFeO_3$ was estimated to be 2.08 V vs RHE. Combined with the bandgap of 2.28 eV, the conduction band minimum (CBM) of the $LaFeO_3$ film was estimated to be -0.2 V vs RHE. As the accuracy of the flatband value determined from Mott-Schottky plot may be debatable due to a possible influence of the surface roughness and the electrolyte [62], a semi-empirical method was also used to confirm the band positions. CBM and VBM values were calculated from Mulliken's electronegativity at point of zero charge using the following equation [63]:

$$E_{VB} = \chi - E^e + 0.5E_g \tag{3}$$

$$E_{CB} = E_{VB} - E_g \tag{4}$$

where E_{VB} and E_{CB} are the VB edge potential and CB edge potential respectively, χ is the absolute electronegativity of the semiconductor on Mulliken's scale (χ = 5.54 for $LaFeO_3$), E^e is the energy of free electrons on the hydrogen scale (4.5 eV vs RHE) and E_g is the bandgap energy estimated from UV-Vis absorption spectra. VBM and CBM positions were estimated to be 2.18 and -0.1 V vs RHE, respectively. These theoretical calculations are in good agreement with Mott-Schottky plots.

VBM and CBM positions of g-C_3N_4 were determined in [47]. The corresponding energy diagram of $LaFeO_3$ and g-C_3N_4 before contact is reported in Fig. 7a. $LaFeO_3$ exhibits VBM and CBM that straddle the redox potential of water. This suggest that $LaFeO_3$ is able to generate hydrogen using visible part of the spectrum without applying any external bias voltage as observed by Pawar et al. [20]. However, the kinetics of production is very low due to the very close position of CB in regards to reduction potential of hydrogen. $LaFeO_3$ associated to g-C_3N_4 will form a p-n heterojunction. PEC efficiency can be greatly influenced by the recombination rate of photo-generated charge carriers and p-n junctions generally promote the effective separation of light-induced electrons and holes. Before contact, CB and Fermi level positions of $LaFeO_3$ are lower than those of g-C_3N_4. At the junction, the Fermi level after contact, under equilibrium conditions, is equal and constant in g-C_3N_4 and $LaFeO_3$, causing an energy band bending. Indeed, after contact between p-type $LaFeO_3$ and n-type g-C_3N_4, electrons diffuse from g-C_3N_4 to $LaFeO_3$ due to the initial positions of CB, leading to an accumulation of negative charges in $LaFeO_3$ close to the junction. At the same time, a positive section in g-C_3N_4 is generated near the junction. As a consequence, the Fermi level and energy band positions of g-C_3N_4 shift downward (to more positive potentials), while those of $LaFeO_3$ shift upward (to more negative potentials) to form an equilibrium state, where an inner electric field is generated and the CB of $LaFeO_3$ is higher than that of g-C_3N_4 (Fig. 7b). Thus, photogenerated electrons on the CB of $LaFeO_3$ will transfer to that of g-C_3N_4. Migration of electrons and holes are promoted by the internal field. Subsequently, the interface of the heterojunction will improve the separation of electron-holes pairs and reduce their recombination probability [64].

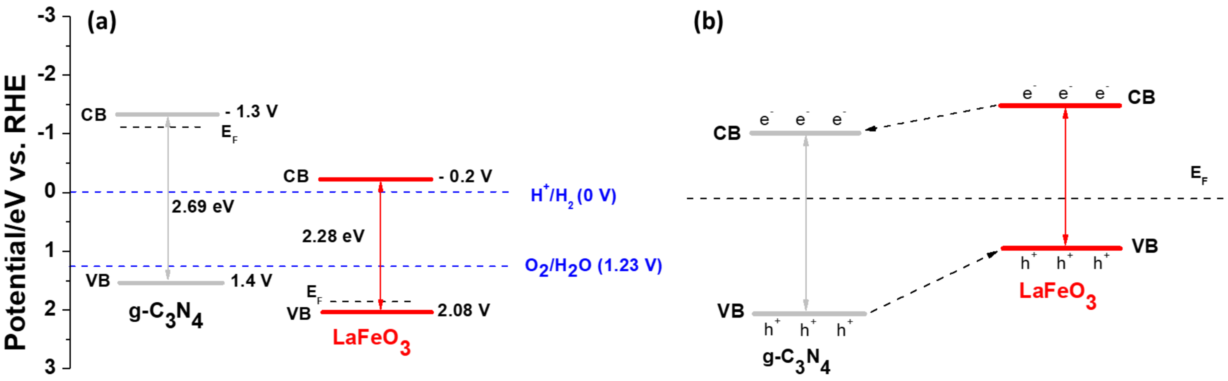

Fig. 7. Schematic diagrams of band energy positions of g-C_3N_4 and $LaFeO_3$ (a) before contact and (b) the proposed electrons/holes transfer and separation processes after contact.

Photoelectrochemical (PEC) analysis

Linear sweep voltammetry (J-V) curves of $LaFeO_3$/g-C_3N_4 were recorded under simulated sunlight illumination (100 mW·cm^{-2}, AM 1.5G), where a chopped beam was used for acquiring both dark current and photocurrent in a single scan at a rate of 5 mV.s^{-1} (Fig. 8a). Each cycle lasts 25 mV. The steady state photocurrent onset potential was around 0.6 V vs RHE and the dark current remained stable until 0.25 V vs RHE.

To determine the $LaFeO_3$ on g-C_3N_4 ratio giving the highest performance, the amount of each material was optimised from chronoamperometric tests under chopped illumination (30 s). The potential was kept constant at -0.3 V versus Ag/AgCl (0.3 V vs RHE) to ensure the minimal impact of dark current in the 0.1 M Na_2SO_4 (pH = 7) electrolyte solution. The photocurrent density varied with the amount of g-C_3N_4 underneath 50 nm-thick $LaFeO_3$ (Fig. 8b). The photoelectrode elaborated using 1 µg of g-C_3N_4 exhibits the highest photocurrent density (4 µA.cm^{-2}). The thickness of the $LaFeO_3$ film deposited on 1 µg of g-C_3N_4 was also found to affect the photocurrent density (Fig. 8c).

Optimal quantities for both materials were thus determined to be a 50 nm thick layer of $LaFeO_3$ deposited on top of 1 µg of g-C_3N_4 with a maximum photocurrent density of 4 µA.cm^{-2}. Spikes and transient photocurrent observed during each period can be attributed to charge carriers recombination. A large number of photoinduced electrons cannot reach the electrolyte before recombining with holes. The photocurrent density becomes stable only when the balance between charge generation, separation, transport and recombination processes is achieved. As expected, thickness of photoelectrode is major parameter that directly impacts the photocurrent density. The electron transport within $LaFeO_3$ is low and charge carriers recombination probability increases with thickness. By contrast, photoactive materials have to be thick enough to ensure light absorption leading to the formation of a high density of electron/hole pairs [65]. The observed higher photocurrent density of $LaFeO_3$/g-C_3N_4 by comparison with $LaFeO_3$ suggests an enhanced charge carriers separation in the heterostructured photoelectrode. Fig. 8d shows the Nyquist plots of EIS spectra for $LaFeO_3$ (50 nm) and optimised $LaFeO_3$/g-C_3N_4 under illumination. The semicircle diameter is related to the charge transfer resistance at the electrode/electrolyte interface. $LaFeO_3$/g-C_3N_4 has a smaller arc diameter than that of $LaFeO_3$, which means a smaller charge transfer resistance. Both photocurrent and EIS results indicate that heterostructured $LaFeO_3$/g-C_3N_4 film exhibits more efficient electron-hole separation under simulated sunlight illumination, mainly due to the electrostatic field in the junction [66].

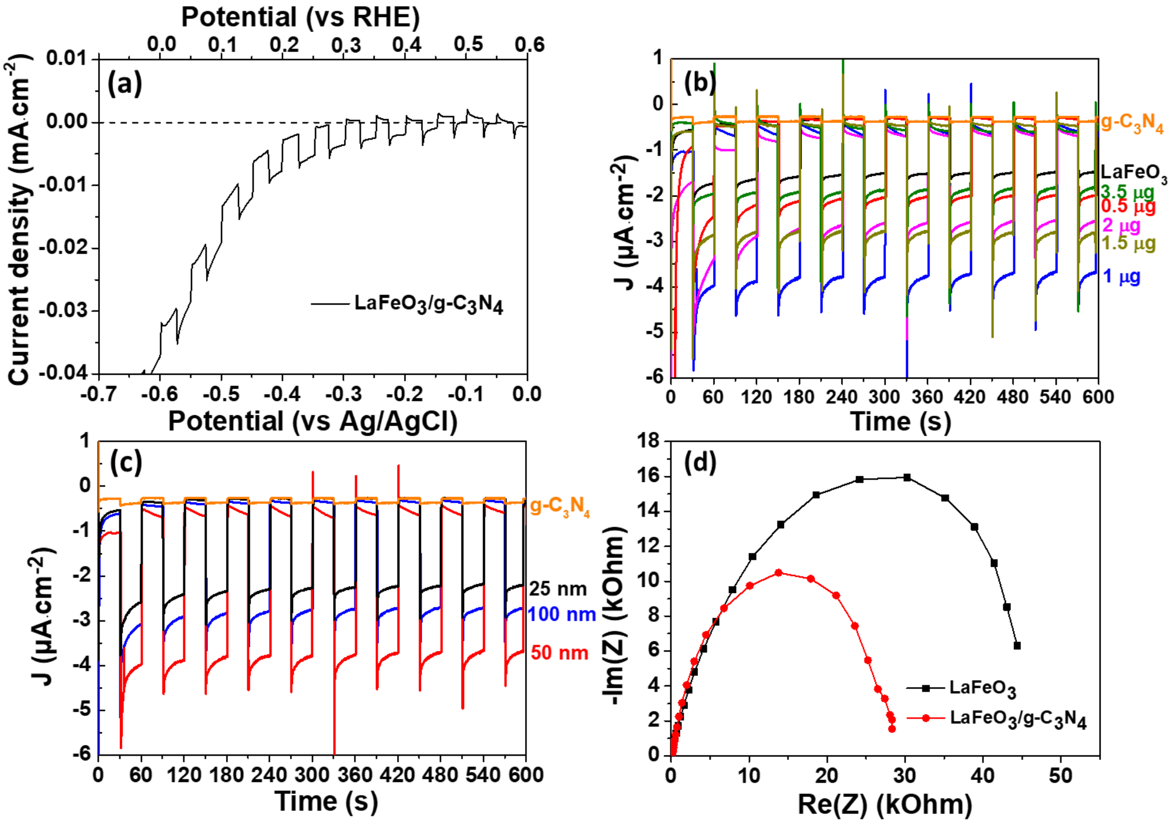

Fig. 8. Current-potential curve (a) and current-time curves of LaFeO$_3$/g-C$_3$N$_4$ heterojunctions at −0.3 V vs Ag/AgCl as a function of (b) the quantity of g-C$_3$N$_4$ spin-coated on FTO (LaFeO$_3$ thickness = 50 nm) and (c) the LaFeO$_3$ film thickness (amount of g-C$_3$N$_4$ = 1 µg) under chopped illumination. (d) EIS Nyquist plots of 50 nm thick LaFeO$_3$ and optimised LaFeO$_3$/g-C$_3$N$_4$ heterostructure (electrolyte: 0.1 M Na$_2$SO$_4$ (pH = 7)).

The stability is a crucial parameter to determine if a system is suitable for practical utilisation. In order to test the stability, a chronoamperometry measurement was conducted for LaFeO$_3$/g-C$_3$N$_4$ heterostructured photocathode at a constant potential of -0.3 V vs Ag/AgCl over a 24 h period under a continuous simulated sunlight illumination in a 0.1 M Na$_2$SO$_4$ electrolyte solution (Fig. 9). After a slight drop in the first 2 h, the current density remained almost constant over the following 22 h (ca. 2.9 µA.cm^{-2}), confirming excellent stability of the photoelectrode. The slight decrease of photocurrent at the beginning of the reaction is generally attributed to the accumulation of gas bubbles at the electrode/electrolyte interface leading to a reduced effective surface area [67]. LaFeO$_3$ and g-C$_3$N$_4$ are promising photoelectrode materials mainly due to their chemical and thermal stability. Moreover, LaFeO$_3$ thin films synthesized by magnetron sputtering have a dense columnar structure with no voids and pores. As a consequence, the electrolyte cannot deeply penetrate in the film and the effective surface area is low, leading to a relatively low photocurrent density. However, the compact nature of the films ensures a good stability of the photoelectrodes by limiting their degradation during a long period of operation. $LaFeO_3$/g-C_3N_4 heterostructured films can thus be used as photocathode for hydrogen production performed over several hours.

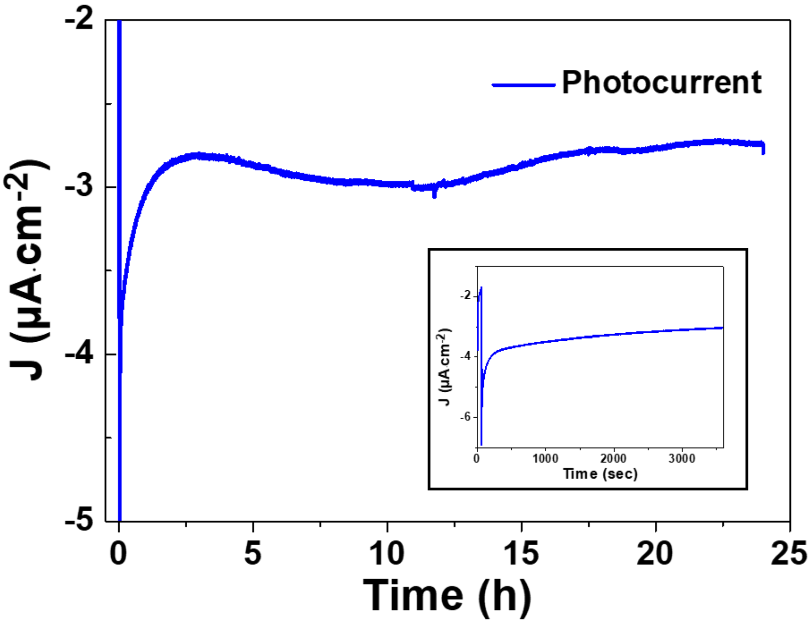

Fig. 9. J-t plot at -0.3V vs Ag/AgCl of 50 nm $LaFeO_3$ deposited over 1 µg of g-C_3N_4, insert is a detail of the first hour.

Hydrogen evolution measurement

Fig. 10a shows the hydrogen production rates of electrodes composed of g-C_3N_4, $LaFeO_3$ and optimized $LaFeO_3$/g-C_3N_4 in an aqueous Na_2SO_4 (pH = 7) electrolyte under a continuous simulated sunlight illumination and at a constant potential of -0.3 V vs Ag/AgCl. The hydrogen production rate was monitored each hour (over 7 h) by mass spectrometry. The cell was first purged with argon for 1 h to ensure that oxygen from air was not involved when the reaction starts. It is worth noting that hydrogen production rates generated by these different photocathodes are in good agreement with current-potential curves. Samples showed very similar hydrogen evolution rates with an initial activation period of about 3 h, followed by a stable and maximum production period. H_2 production rates of g-C_3N_4, $LaFeO_3$ and $LaFeO_3$/g-C_3N_4 in the steady states are 5.5, 6.2 and 10.8 µmol.h^{-1}.cm^{-2}, respectively. As a consequence, an increase of 74% in H_2 production rate is observed by depositing a g-C_3N_4 sublayer underneath $LaFeO_3$ thin film. To determine the stability of $LaFeO_3$/g-C_3N_4 heterostructured film, sample underwent 3 cycles of water splitting test (Fig. 10b). These results provide additional evidence that the film is reusable although a decrease of 30% is observed after the third cycle.

Based on the previously described experimental results, a possible mechanism can be proposed for the photogenerated charges separation and the PEC water splitting process (Fig. 10c). Under visible light irradiation, both g-C_3N_4 and $LaFeO_3$ absorb photons and electron-hole pairs are generated. In the heterostructured film, photo-excited electrons in the CB of g-C_3N_4 can transfer to the CB of $LaFeO_3$ while holes in the VB of $LaFeO_3$ move to the VB of g-C_3N_4, thus facilitating the separation of electron/hole pairs. In the overall PEC process, the reaction of hydroxyl anions OH^- (or H_2O) at the Pt counter electrode will produce electrons that can combine with holes in the VB of g-C_3N_4. Due to their more positive potential than the H^+/H_2 couple, the electrons in the CB of $LaFeO_3$ can reduce H^+ into H_2. The $LaFeO_3$/g-C_3N_4 photocathode benefits from the efficient charge carrier separation and exhibits a high PEC water splitting efficiency.

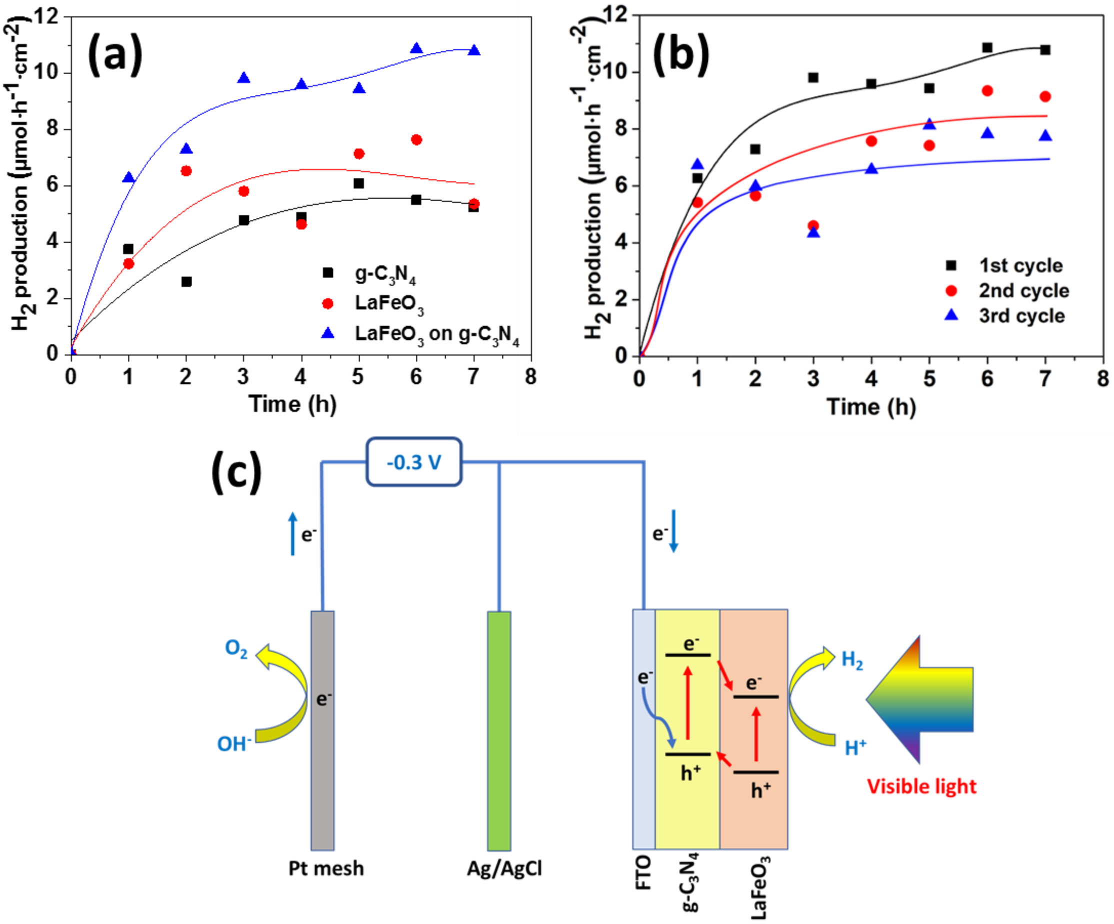

Fig. 10. (a) Hydrogen production rate of $LaFeO_3$, $g\text{-}C_3N_4$ and $LaFeO_3/g\text{-}C_3N_4$ photoelectrodes and (b) stability performances of $LaFeO_3/g\text{-}C_3N_4$ heterostructured film over 3 cycles (-0.3 V vs Ag/AgCl, 0.1 M Na_2SO_4, 100 $mW.cm^{-2}$ – AM1.5G) and (c) Schematic illustration of the electron transfer pathway for visible light PEC hydrogen production using $LaFeO_3/g\text{-}C_3N_4$ films.

Conclusion

For the first time, a thin $LaFeO_3$ film was deposited using magnetron sputtering and associated with $g\text{-}C_3N_4$ for PEC hydrogen production. $g\text{-}C_3N_4$ was deposited directly on the substrate, prior to $LaFeO_3$, using a simple spin-coating method. Deposition of a sublayer of $g\text{-}C_3N_4$ improves the separation of charge carriers at the $LaFeO_3/g\text{-}C_3N_4$ interface, while optical properties of $LaFeO_3$ still allows it to absorb a large range of the visible spectra, increasing its efficiency. Optimal quantities of both materials were determined using chronoamperometry. Subsequently, water splitting test was performed to estimate the photocatalytic properties of the g-C_3N_4/$LaFeO_3$ heterojunction to produce hydrogen. Associating $LaFeO_3$ with g-C_3N_4 led to hydrogen production rate of 10.8 $\mu mol \cdot h^{-1} \cdot cm^{-2}$ and to an increased amount of produced hydrogen by 74% compared to pure $LaFeO_3$. The hydrogen production remains high after three reuses, demonstrating the stability of the g-C_3N_4/$LaFeO_3$ film after further cycles of production and its ability to harvest light for days. Our work thus demonstrates a simple route to obtain well performant heterostructured materials systems for hydrogen production from low-cost, non-toxic and abundant components.

Acknowledgements

This work was supported partly by the French PIA project « Lorraine Université d'Excellence », reference ANR-15-IDEX-04-LUE.

Appendix A. Supplementary data

Supplementary data to this article can be found at http://doi.org/

References

[1] Mazloomi K, Gomes C. Hydrogen as an energy carrier: prospects and challenges. Renew Sust Energ Rev 2012;16:3024–33. https://doi.org/10.1016/j.rser.2012.02.028.
[2] Züttel A, Remhof A, Borgschulte A, Friedrichs O. Hydrogen: the future energy carrier. Philos Trans A Math Phys Eng Sci 2010;368:3329–42. https://doi.org/10.1098/rsta.2010.0113.
[3] Ewan BCR, Allen RWK. A figure of merit assessment of the routes to hydrogen. Int J Hydrog Energy 2005;30:809–819. https://doi.org/10.1016/j.ijhydene.2005.02.003.
[4] Acar C, Dincer I, Naterer GF. Review of photocatalytic water-splitting methods for sustainable hydrogen production. Int J Energy Res 2016;40:1449-1473.
[5] Fajrina N, Tahir M. A critical review in strategies to improve photocatalytic water splitting towards hydrogen production. Int J Hydrog Energy 2019;44:540-577. https://doi.org/10.1016/j.ijhydene.2018.10.200
[6] Fushijima A,Honda K. Electrochemical photolysis of water at a semiconductor electrode. Nature 1972;238:37–38. https://doi.org/10.1038/238037a0.
[7] Grätzel M. Photoelectrochemical cells. Nature 2001;414:338–44. https://doi.org/10.1038/35104607.

[8] Lin Y, Yuan G, Liu R, Zhou S, Sheehan SW, Wang D. Semiconductor nanostructure-based photoelectrochemical water splitting: a brief review. Chem Phys Lett 2011;507:209–15. https://doi.org/10.1016/j.cplett.2011.03.074.

[9] Wang R, Yan J, Zu M, Yang S, Cai X, Gao Q, Fang Y, Zhang S, Zhang S. Facile synthesis of interlocking g-C_3N_4/CdS photoanode for stable photoelectrochemical hydrogen production. Electrochim Acta 2018;279:74-83. https://doi.org/10.1016/j.electacta.2018.05.076

[10] Zhang S, Yan J, Yang S, Xu Y, Cai X, Li X, Zhang X, Peng F, Fang Y. Electrodeposition of Cu_2O/g-C_3N_4 heterojunction film on an FTO substrate for enhancing visible light photoelectrochemical water splitting. Chinese J Catal 2017;38:365–371. https://doi.org/10.1016/S1872-2067(16)62588-3

[11] Yu Y, Zhang Z, Yin X, Kvit A, Liao Q, Kang Z, Yan X, Zhang Y, Wang X. Enhanced photoelectrochemical efficiency and stability using a conformal TiO_2 film on a black silicon photoanode. Nat Energy 2017;2:17045. https://doi.org/10.1038/nenergy.2017.45.

[12] Wolcott A, Smith WA, Kuykendall TR, Zhao Y, Zhang JZ. Photoelectrochemical study of nanostructured ZnO thin films for hydrogen generation from water splitting. Adv Funct Mater 2009;19:1849–56. https://doi.org/10.1002/adfm.200801363.

[13] Acar C, Dincer I, Naterer GF. Review of photocatalytic water-splitting methods for sustainable hydrogen production. Int J Energy Res 2016;40:1449–73. https://doi.org/10.1002/er.3549.

[14] Kumaravel V, Mathew S, Bartlett J, Pillai SC. Photocatalytic hydrogen production using metal doped TiO_2: a review of recent advances. Appl Catal B 2019;244:1021–64. https://doi.org/10.1016/j.apcatb.2018.11.080.

[15] Cai J, Shen J, Zhang X, Ng YH, Huang j, Guo W, Lin C, Lai Y. Light-driven sustainable hydrogen production utilizing TiO_2 nanostructures: a review. Small Methods 2019;3:1800184. https://doi.org/10.1002/smtd.201800184.

[16] Wheeler GP, Choi KS. Photoelectrochemical properties and stability of nanoporous p-type $LaFeO_3$ photoelectrodes prepared by electrodeposition. ACS Energy Lett 2017;2:2378–82. https://doi.org/10.1021/acsenergylett.7b00642.

[17] Parida KM, Reddy KH, Martha S, Das DP, Biswal N. Fabrication of nanocrystalline $LaFeO_3$: an efficient sol–gel auto-combustion assisted visible light responsive photocatalyst for water decomposition. Int J Hydrog Energy 2010;35:12161–8. https://doi.org/10.1016/j.ijhydene.2010.08.029.

[18] Celorrio V, Bradley K, Weber OJ, Hall SR, Fermín DJ. Photoelectrochemical properties of $LaFeO_3$ nanoparticles. ChemElectroChem 2014;1:1667–71. https://doi.org/10.1002/celc.201402192.

[19] Díez-García MI, Gómez R. Metal doping to enhance the photoelectrochemical behavior of $LaFeO_3$ photocathodes. ChemSusChem 2017;10:2457–63. https://doi.org/10.1002/cssc.201700166.

[20] Pawar GS, Tahir AA. Unbiased spontaneous solar fuel production using stable $LaFeO_3$ photoelectrode. Sci Rep 2018;8:3501. https://doi.org/10.1038/s41598-018-21821-z.

[21] Pawar GS, Elikkottil A, Seetha S, Reddy KS, Pesala B, Tahir AA, Mallick TK. Enhanced photoactivity and hydrogen generation of $LaFeO_3$ photocathode by plasmonic silver nanoparticle incorporation. ACS Appl Energy Mater 2018;1:3449–56. https://doi.org/10.1021/acsaem.8b00628.

[22] Jaouali I, Hamrouni H, Moussa N, Nsib MF, Centeno MA, Bonavita A, Neri G, Leonardi SG. $LaFeO_3$ ceramics as selective oxygen sensors at mild temperature. Ceram Int 2018;44:4183–89. https://doi.org/10.1016/j.ceramint.2017.11.221.

[23] Barbero BP, Gamboa JA, Cadús LE. Synthesis and characterisation of $La_{1-x}Ca_xFeO_3$ perovskite-type oxide catalysts for total oxidation of volatile organic compounds. Appl Catal B 2006;65:21–30. https://doi.org/10.1016/j.apcatb.2005.11.018.

[24] Anajafi Z, Naseri M, Neri G. Optical, magnetic and gas sensing properties of $LaFeO_3$ nanoparticles synthesized by different chemical methods. J Electron Mater 2019;48:6503-11. https://doi.org/10.1007/s11664-019-07436-8.

[25] Peng Q, Wang J, Wen YW, Shan B, Chen R. Surface modification of $LaFeO_3$ by Co-Pi electrochemical deposition as an efficient photoanode under visible light. RSC Adv 2016;6:26192–8. https://doi.org/10.1039/C6RA01810F.

[26] Li S, Jing L, Fu W, Yang L, Xin B, Fu H. Photoinduced charge property of nanosized perovskite-type $LaFeO_3$ and its relationships with photocatalytic activity under visible irradiation. Mater Res Bull 2007;42:203–12. https://doi.org/10.1016/j.materresbull.2006.06.010.

[27] Hu R, Li C, Wang X, Sun Y, Jia H, Su H, Zhang Y. Photocatalytic activities of $LaFeO_3$ and La_2FeTiO_6 in p-chlorophenol degradation under visible light. Catal Commun 2012;29:35–39. https://doi.org/10.1016/j.catcom.2012.09.012.

[28] Thirumalairajan S, Girija K, Hebalkar NY, Mangalaraj D, Viswanathan C, Ponpandian N. Shape evolution of perovskite $LaFeO_3$ nanostructures: a systematic investigation of growth mechanism, properties and morphology dependent photocatalytic activities. RSC Adv 2013;3:7549–61. https://doi.org/10.1039/C3RA00006K.

[29] Li J, Pan X, Xu Y, Jia L, Yi X, Fang W. Synergetic effect of copper species as cocatalyst on $LaFeO_3$ for enhanced visible-light photocatalytic hydrogen evolution. Int J Hydrog Energy 2015;40:13918–25. https://doi.org/10.1016/j.ijhydene.2015.07.166.

[30] Ismael M, Wark M. Perovskite-type $LaFeO_3$: photoelectrochemical properties and photocatalytic degradation of organic pollutants under visible light irradiation. Catalysts 2019;9:342. https://doi.org/10.3390/catal9040342.

[31] Ren X, Yang H, Gen S, Zhou J, Yang T, Zhang X, Cheng Z, Sun S. Controlled growth of $LaFeO_3$ nanoparticles on reduced graphene oxide for highly efficient photocatalysis. Nanoscale 2016;8:752–6. https://doi.org/10.1039/C5NR06338H.

[32] Humayun M, Qu Y, Raziq F, Yan R, Li Z, Zhang X, Jing L. Exceptional visible-light activities of TiO_2-coupled N-doped porous perovskite $LaFeO_3$ for 2,4-dichlorophenol decomposition and CO_2 conversion. Environ Sci Technol 2016;50:13600–10. https://doi.org/10.1021/acs.est.6b04958.

[33] Gong C, Zhang Z, Lin S, Wu Z, Sun L, Ye C, Hu Y, Lin C. Electrochemical synthesis of perovskite $LaFeO_3$ nanoparticle-modified TiO_2 nanotube arrays for enhanced visible-light photocatalytic activity. New J Chem 2019;43:16506–14. https://doi.org/10.1039/C9NJ03908B.

[34] Xu K, Xu H, Feng G, Feng J. Photocatalytic hydrogen evolution performance of NiS cocatalyst modified $LaFeO_3$/g-C_3N_4 heterojunctions. New J Chem 2017;41:14602–9. https://doi.org/10.1039/C7NJ03120C.

[35] Rakibuddin M, Kim H, Ehtisham Khan M. Graphite-like carbon nitride (C_3N_4) modified N-doped $LaTiO_3$ nanocomposite for higher visible light photocatalytic and photo-electrochemical performance. Appl Surf Sci 2018;452:00–412. https://doi.org/10.1016/j.apsusc.2018.05.018.

[36] Jin L, Zhou X, Ning X, Zhan L, Kong M, Tan K, Li J, Lin Z. Boosting visible light photocatalytic performance of g-C_3N_4 nanosheets by combining with $LaFeO_3$ nanoparticles. Mater Res Bull 2018;102:353–61. https://doi.org/10.1016/j.materresbull.2018.02.057.

[37] Wu Y, Wang H, Tu W, Liu Y, Tan YZ, Yuan X, Chew JW. Quasi-polymeric construction of stable perovskite-type $LaFeO_3$/g-C_3N_4 heterostructured photocatalyst for improved Z-scheme photocatalytic activity via solid p-n heterojunction interfacial effect. J Hazard Mater 2018;347:412–22. https://doi.org/10.1016/j.jhazmat.2018.01.025.

[38] Ye Y, Yang H, Wang X, Feng W. Photocatalytic, fenton and photo-fenton degradation of RhB over Z-scheme g-C_3N_4/$LaFeO_3$ heterojunction photocatalysts. Mater Sci Semicond Process 2018;82:14–24. https://doi.org/10.1016/j.mssp.2018.03.033.

[39] Gao X, Shang Y, Liu L, Nie W. A plasmonic Z-scheme three-component photocatalyst g-C_3N_4/Ag/$LaFeO_3$ with enhanced visible-light photocatalytic activities. Opt Mater 2019;88:229–37. https://doi.org/10.1016/j.optmat.2018.11.030.

[40] Ibarra-Rodriguez LI, Huerta-Flores AM, Torres-Martínez LM. Facile synthesis of g-C_3N_4/ $LaMO_3$ (M: Co, Mn, Fe) composites for enhanced visible-light-driven photocatalytic water splitting. Mater Sci Semicond Process 2019;103:104643. https://doi.org/10.1016/j.mssp.2019.104643.

[41] Acharya S, Mansingh S, Parida KM. The enhanced photocatalytic activity of g-C_3N_4-$LaFeO_3$ for the water reduction reaction through a mediator free Z-scheme mechanism. Inorg Chem Front 2017;4:1022–32. https://doi.org/10.1039/C7QI00115K.

[42] Ye S, Wang R, Wu MZ, Yuan YP. A review on g-C_3N_4 for photocatalytic water splitting and CO_2 reduction. Appl Surf Sci 2015;358:15–27. https://doi.org/10.1016/j.apsusc.2015.08.173.

[43] Wen J, Xie J, Chen X, Li X. A review on g-C_3N_4-based photocatalysts. Appl Surf Sci 2017;391:72–123. https://doi.org/10.1016/j.apsusc.2016.07.030.

[44] Fu J, Yu J, Jiang C, Cheng B. g-C_3N_4-based heterostructured photocatalysts. Adv Energy Mater 2018;8:1701503. https://doi.org/10.1002/aenm.201701503.

[45] Mishra A, Mehta A, Basu S, Shetti NP, Reddy KR, Aminabhavi TM. Graphitic carbon nitride (g–C_3N_4)–based metal-free photocatalysts for water splitting: a review. Carbon 2019;149:693–721. https://doi.org/10.1016/j.carbon.2019.04.104.

[46] Moussa H, Chouchene B, Gries T, Balan L, Mozet K, Medjahdi G, Schneider R. Growth of ZnO nanorods on graphitic carbon nitride gCN sheets for the preparation of photocatalysts with high visible-light activity. ChemCatChem 2018;10:4973–83. https://doi.org/10.1002/cctc.201801206.

[47] Ben Abdelaziz M, Chouchene B, Balan L, Gries T, Medjahdi G, Ezzaouia H, Schneider R. One pot synthesis of bismuth oxide/graphitic carbon nitride composites with high photocatalytic activity. Mol Catal 2019;463:110–8. https://doi.org/10.1016/j.mcat.2018.12.004.

[48] Ouedraogo S, Chouchene B, Desmarets C, Gries T, Balan L, Fournet R, Medjahdi G, Bayo K, Schneider R. Copper octacarboxyphthalocyanine as sensitizer of graphitic carbon nitride for efficient dye degradation under visible light irradiation. Appl Catal A 2018;563:127–36. https://doi.org/10.1016/j.apcata.2018.06.036.

[49] Li X, Zhang J, Shen L, Ma Y, Lei W, Cui Q, Zou G. Preparation and characterization of graphitic carbon nitride through pyrolysis of melamine. Appl Phys A 2009;94:387–92. https://doi.org/10.1007/s00339-008-4816-4.

[50] Xiang Q, Yu J, Jaroniec M. Preparation and enhanced visible-light photocatalytic H_2-production activity of graphene/C_3N_4 composites. J Phys Chem C 2011;115:7355–63. https://doi.org/10.1021/jp200953k.

[51] Tang P, Tong Y, Chen H, Cao F, Pan G. Microwave-assisted synthesis of nanoparticulate perovskite $LaFeO_3$ as a high active visible-light photocatalyst. Curr Appl Phys 2013;13:340–3. https://doi.org/10.1016/j.cap.2012.08.006.

[52] Dhinesh Kumar R, Jayavel R. Facile hydrothermal synthesis and characterization of $LaFeO_3$ nanospheres for visible light photocatalytic applications. J Mater Sci: Mater Electron 2014;25:3953–61. https://doi.org/10.1007/s10854-014-2113-x.

[53] Wang X, Maeda K, Thomas A, Takanabe K, Xin G, Carlsson JM, Domen K, Antonietti M. A metal-free polymeric photocatalyst for hydrogen production from water under visible light. Nat Mater 2008;8:76-80. https://doi.org/10.1038/nmat2317.

[54] Geller S, Wood EA. Crystallographic studies of perovskite-like compounds. I. Rare earth orthoferrites and $YFeO_3$, $YCrO_3$, $YAlO_3$. Acta Cryst 1956;9:563–8. https://doi.org/10.1107/S0365110X56001571.

[55] Venugopalan S, Becker MM. Raman scattering study of $LuFeO_3$. J Chem Phys 1990;93:3833–6. https://doi.org/10.1063/1.458768.

[56] Wang PN, Guo Z, Ying XT, Chen JH, Xu XM, Li FM. Raman spectroscopy on the $\beta-C_3N_4$ structure formed by low-energy nitrogen ion implantation into a diamond surface. Phys Rev B 1999;59:13347–9. https://doi.org/10.1103/PhysRevB.59.13347.

[57] Peng K, Fu L, Yang H, Ouyang J. Perovskite $LaFeO_3$/montmorillonite nanocomposites: synthesis, interface characteristics and enhanced photocatalytic activity. Sci Rep 2016;6:19723. https://doi.org/10.1038/srep19723.

[58] Davis EA, Mott NF. Conduction in non-crystalline systems V. Conductivity, optical absorption and photoconductivity in amorphous semiconductors. Philos Mag 1970;22:0903–22. https://doi.org/10.1080/14786437008221061.

[59] Scafetta MD, Cordi AM, Rondinelli JM, May SJ. Band structure and optical transitions in $LaFeO_3$: theory and experiment. J Phys Condens Matter 2014;26:505502. https://doi.org/10.1088/0953-8984/26/50/505502.

[60] Köferstein R, Jäger L, Ebbinghaus SG. Magnetic and optical investigations on $LaFeO_3$ powders with different particle sizes and corresponding ceramics. Solid State Ion 2013;249–250:1–5. https://doi.org/10.1016/j.ssi.2013.07.001.

[61] Gelderman K, Lee L, Donne SW. Flat-band potential of a semiconductor: using the Mott–Schottky equation. J Chem Educ 2007;84:685. https://doi.org/10.1021/ed084p685.

[62] Hamann TW, Gstrein F, Brunschwig BS, Lewis NS. Measurement of the dependence of interfacial charge-transfer rate constants on the reorganization energy of redox species at n-ZnO/H_2O interfaces. J Am Chem Soc 2005;127:13949–54. https://doi.org/10.1021/ja0515452.

[63] Lu P, Hu X, Li Y, Peng Y, Zhang M, Jiang X, He Y, Fu M, Dong F, Zhang Z. Novel $CaCO_3$/g-C_3N_4 composites with enhanced charge separation and photocatalytic activity. J Saudi Chem Soc 2019;23:1109-18. https://doi.org/10.1016/j.jscs.2019.07.002.

[64] Liang Q, Jin J, Liu C, Xu S, Li Z. Constructing a novel p-n heterojunction photocatalyst $LaFeO_3$ /g-C_3N_4 with enhanced visible-light-driven photocatalytic activity. J Alloys Compd 2017;709:542–8. https://doi.org/10.1016/j.jallcom.2017.03.190.

[65] May KJ, Fenning DP, Ming T, Hong WT, Lee D, Stoerzinger KA, Biegalski MD, Kolpak AM, Shao-Horn Y. Thickness-dependent photoelectrochemical water splitting on ultrathin

$LaFeO_3$ films grown on Nb:$SrTiO_3$. J Phys Chem Lett 2015;6:977–85. https://doi.org/10.1021/acs.jpclett.5b00169.

[66] Yang J, Hu R, Meng W, Du Y. A novel p-$LaFeO_3$/n-Ag_3PO_4 heterojunction photocatalyst for phenol degradation under visible light irradiation. Chem Commun 2016;52:2620–3. https://doi.org/10.1039/C5CC09222A.

[67] Hernández S, Barbero G, Saracco G, Alexe-Ionescu AL. Considerations on oxygen bubble formation and evolution on $BiVO_4$ porous anodes used in water splitting photoelectrochemical cells. J Phys Chem C 2015;119:9916–25. https://doi.org/10.1021/acs.jpcc.5b01635.